Magnetron sputtering of Ti_2O_3 films

Authors: Petr V. Shvets[a,b*], David Caffrey[b], Karsten Fleischer[b,c], Igor Shvets[b], Ksenia Yu. Maksimova[a], and Alexander Yu. Goikhman[a]

Affiliations: [a]REC "Functional Nanomaterials", Immanuel Kant Baltic Federal University, Kaliningrad, Russian Federation

[b]School of Physics, Trinity College Dublin, Dublin 2, Ireland

[c]School of Physical Sciences, Dublin City University, Dublin 9, Ireland

*corresponding author, e-mail: pshvets@innopark.kantiana.ru

Declarations of interest: none.

Abstract. We report on the synthesis of titanium suboxide films using a magnetron sputtering setup. The structure of the produced films is characterized using Raman spectroscopy and X-ray diffraction and electrical properties are measured by four-probe method. We demonstrate that depending on the oxidation rate of the growing films it is possible to produce polycrystalline α-TiO, corundum and orthorhombic Ti_2O_3 or almost amorphous TiO_2. We focus on the characterization of the two phases of Ti_2O_3 and show that their structure and electrical properties significantly differ from earlier results obtained for bulk crystals or epitaxial films. Our corundum-type Ti_2O_3 films have high electrical conductivity (compared to the bulk) and no metal-insulator phase transition: the material is locked in the metallic state. The conductivity of our orthorhombic Ti_2O_3 is lower compared to epitaxial films; this phase does not demonstrate any phase transitions as well.

Keywords: Titanium suboxides, Ti_2O_3, Magnetron sputtering, Thin films, Raman scattering, TiO, Metal-insulator phase transitions.

1. Introduction

The first report on titanium sesquioxide (titanium III oxide, or Ti_2O_3) crystal structure was published more than 90 years ago [1]. This material normally crystallizes into corundum-type space group $R\bar{3}c$ with lattice parameters of a = 5.157 Å and c = 13.61 Å. Ti_2O_3 attracted some interest due to a broad semiconductor to metal phase transition in the temperature range of 150–300 °C [2, 3]. This transition is accompanied by a rapid change of physical properties such as electrical resistivity [4], specific heat [5], elastic constants [6], and magnetic susceptibility [7]. Very recently it was shown that nanoparticle-based Ti_2O_3 films could be used as an efficient photothermal material promising for seawater desalination and purification [8].

Under high pressures and high temperatures (19 GPa and 1850 K) corundum Ti_2O_3 phase transforms into golden semiconducting Th_2S_3-type structure, which is fully quenchable to ambient conditions (*Pnma* orthorhombic cell, a = 7.82 Å, b = 2.85 Å, c = 8.12 Å at ambient conditions) [9, 10].

Recently, it was shown that Ti_2O_3 could crystallize into another space group, *Immm*, with orthorhombic cell parameters of a = 9.39 Å, b = 4.42 Å and c = 2.81 Å. The material was obtained as an epitaxial thin film on (0001) sapphire substrate using pulsed laser deposition and Ti_2O_3 target at substrate temperatures above 700 °C [11]. Such films are ferromagnetic n-type semiconductors with a very high electron concentration and they also demonstrate a semiconductor to metal transition at about 370 K. The synthesis of the same material by cathodic arc sputtering was reported in our previous article, but that time the phase was not properly identified and characterized [12].

In most studies, titanium suboxides are produced by different chemical methods, including carbothermic [13], metallothermic [14] or hydrogen [15] reduction of TiO_2 or by oxidizing different titanium-containing precursors, such as $TiCl_3$ [16], TiH_2 [17], titanium-tetra-isopropoxide [18], and others. These methods usually lead to the formation of the bulk or powder samples. Thin films are mainly produced by the sputtering of titanium targets or chemical vapor

deposition, but the reports on the formation and properties of such phases as Ti_2O, TiO, Ti_2O_3, Ti_3O_5, or Ti_4O_7 are very limited [11, 12, 19–21]. In this work, we demonstrate the formation of thin films of different titanium oxide phases with a focus on the structural and electrical characterization of the produced Ti_2O_3 samples.

2. Experimental details

Titanium oxide films were deposited using magnetron sputtering system (AJA international A3200-XP sources). The base pressure in the vacuum chamber was about 10^{-5} mbar and the typical pressure of Ar / O_2 mixture during the growth was $4.5x10^{-3}$ mbar. Ti_2O_3 samples were produced both by reactive RF sputtering from a metallic Ti target (Kurt J Lesker 99.99% purity) and by sputtering from a ceramic Ti_2O_3 target (Kurt J Lesker 99.99% purity) in a pure argon atmosphere. Reactive sputtering rate was monitored in-situ using an Inficon quartz crystal monitor. This allowed for estimation of the sample thickness and also ensured that deposition conditions were consistent. All reactive samples were grown in metallic mode with the oxygen partial pressure below the oxide point. During the deposition, the substrate could be heated to temperatures of up to 800 °C. The typical deposition time was one hour leading to the formation of 250–900 nm thick films depending on the target material and applied power rate (100–200 W) and type (DC or RF). The samples were deposited on glass or Si (100) // SiO_2 (100 nm) substrates.

The crystal structure of the produced samples was determined by X-ray diffraction (XRD) using Bruker AXS D8 DISCOVER setup with a Cu Kα (0.15418 nm) radiation monochromised by a Ge double bounce monochromator in θ–2θ geometry over the range of 20–90 degrees. The lattice constants of the crystals were calculated using the least squares method by minimizing the following expressions:

$$F_1 = \sum_i \left(\frac{4}{3a^2}(h_i^2 + h_i * k_i + k_i^2) + \frac{l_i^2}{c^2} - \frac{1}{d_i^2} \right)^2$$

for the $R\bar{3}c$ space group, and

$$F_2 = \sum_i \left(\frac{h_i^2}{a^2} + \frac{k_i^2}{b^2} + \frac{l_i^2}{c^2} - \frac{1}{d_i^2} \right)^2$$

for the *Immm* space group, where h_i, k_i and l_i are the Miller indices corresponding to all observed peaks, d_i are the corresponding interplane distances, and a, b and c are the lattice constants of the crystal. Crystallographic domain sizes were calculated from the FWHM of the XRD patterns using the Scherrer equation.

Additional structural investigations were performed using Horiba Jobin Yvon micro-Raman spectrometer LabRam HR800 with x100 magnification lens in the range of 65–865 cm^{-1}. A He-Ne laser with 632.8 nm wavelength was used to excite the Raman scattering. The laser was focused at a spot with a diameter of about 300 μm and the irradiation power was limited to approximately 2 mW to avoid any structural changes or phase degradation of the samples.

The electrical characterization of the samples was performed through four-probe method. For the low-temperature regime (5–300 K), measurements were performed using a Keithley 2400 sourcemeter in Van de Paul geometry using silver wire contacted through silver adhesive to the sample surface under evacuation and closed cycle refrigeration. At elevated temperatures (300–600 K) the same sourcemeter was used but a linear 4-point probe measurement was made using spring loaded gold contacts. Elevated temperatures were achieved through the use of a resistive heater placed below the sample substrate. Temperature control was maintained by proportional-integral-derivative (PID) control of the heater power with a thermocouple attached to the resistive heater as feedback. Prior to measurement of the high temperature behavior the system was sealed in a bell jar, which was evacuated and then back filled with nitrogen five times to produce an oxygen deficient environment. This was done to minimize reaction with atmospheric oxygen at high temperatures.

3. Results and discussion

3.1. Corundum Ti_2O_3 films produced by reactive sputtering.

Stoichiometric Ti_2O_3 samples could be produced by reactive magnetron sputtering in

oxygen when the film growth rate to reactive gas pressure is about 50 nm / (min*μbar) and substrate temperature is between 550 and 600 °C. The typical XRD pattern for such film (510 nm thickness: 60 min of 200 W RF sputtering; argon to oxygen pressure: 4.32 : 0.18 μbar; substrate temperature: 550 °C) deposited on glass substrate is shown in Figure 1. The indexing is done by comparing of our pattern to one calculated from the structural file CIF#1532065 (Crystallography Open Database (COD), [22]).

All observed peaks could be attributed to Ti_2O_3 crystal ($R\bar{3}c$ space group) with lattice constants of c = 13.87 Å and a = 5.07 Å. Compared to the bulk, our films are expanded along c-direction and contracted along the a-direction, similarly to the effect observed in Ti_2O_3 nanoparticles [23]. On the other hand, the same structural changes could be observed by heating of Ti_2O_3 single crystals [2]. For instance, a similar c = 13.87 Å can be achieved for bulk samples at T ≈ 340°C, significantly above the phase transition temperature. This indicates, that the structure of our thin films at room temperature corresponds to the structure of bulk Ti_2O_3 in the high temperature, metallic phase. The average coherent crystallographic domain size for the thin films is 40 nm, much smaller than the film thickness. The presence of a significant amount of grain boundaries could therefore be the driving force for the phase stabilisation of the metallic state.

The distortion of the crystal structure is also seen in Raman spectra of the samples (see Figure 2). The typical spectrum consists of seven lines, corresponding to a full set of A_{1g} and E_g vibrations of the Ti_2O_3 crystal lattice [3]. All are shifted towards the lower wavenumbers compared to the bulk: 210, 256, 298, 339, 449, 503, and 559 cm^{-1} instead of 237.5, 279, 306, 350, 466, 514, and 571 cm^{-1}. Moreover, the intensities of the first A_{1g} and the first E_g lines are almost the same, while in bulk samples, and 632.8 nm excitation wavelength, the first A_{1g} mode was previously reported to be about five times stronger than the first E_g mode [24]. Such redshift and change in relative intensities can also be observed during the heating of the bulk crystal above the metal-insulator transition temperature. This, again, supports the assumption of the

metallic nature of our films at room temperature.

All reactively sputtered Ti_2O_3 films exhibit the similar behavior, even at the edges of stability (where Ti_2O_3 is mixed with other phases), with lattice constants in the range of c = 13.8 – 13.9 Å and a = 5.02 – 5.08 Å giving c/a = 2.72 – 2.76 that is well above the value corresponding to the semiconductor to metal transition region (c/a = 2.68 – 2.70, [2]). The recent calculation [25] showed that this ratio plays the major role on the width of the bandgap, thus we could expect that the conductivity of our samples would correspond to the conductivity of the bulk at elevated temperatures (above the phase transition region). Our measurements confirmed such behavior (see Figure 3). We should also note that Ti_2O_3 films demonstrate no rapid change of resistivity neither at high nor at low temperatures. This indicates that the films are "frozen" into the metallic state. The observed increase of conductivity with temperature for our films, contrary to what is expected in a metal, could be associated with contributions of grain boundaries material, or overall defective nature of the thin films. A strong defect or grain boundary scattering contribution in a metal can lead to the observed conductivity improvements with temperature, as their effect is reduced at higher temperatures. We relate the absence of the phase transition to the significant decrease of the lattice constant a for our films compared to the bulk, where it varies from 5.157 to 5.125 Å for temperatures between 20 and 600 °C [2]. An alternative explanation is the low crystallographic domain size observed in the films, which leads to a high number of grain boundaries within the films. The high number of such boundaries could lead to the suppression of the transition behavior due to frequent disruption of the Ti-Ti bond which is the origin of the behavior. Both mechanisms, the lattice distortion and small grain size are most likely linked.

3.2. Other titanium oxide phases produced by reactive sputtering.

The amount of oxygen in the growing film is determined by the oxygen pressure inside the chamber, the rate of target sputtering, the surface state of the target (metallic vs. compound sputtering) and the substrate temperature. Depending on the conditions, the following phases

could be reactively sputtered from the titanium target (in the order of increasing oxygen partial pressure during growth): TiO – orthorhombic (*Immm*) Ti_2O_3 – corundum ($R\bar{3}c$) Ti_2O_3 – anatase TiO_2 – rutile TiO_2. The same sequence was previously observed using an arc sputtering technique [12]. During the magnetron reactive sputtering, *Immm* Ti_2O_3 was always mixed with either TiO, or $R\bar{3}c$ Ti_2O_3, or both. The pure phase was produced from Ti_2O_3 target and will be characterized in detail in the following chapter.

XRD patterns of the selected TiO_x films are given in Figure 4 and the corresponding Raman spectra are shown in Figure 5. The amount of oxygen in a film is increasing from sample (a) to sample (d); the list of growth parameters is given in Table 1. The indexing in Figure 4 is done by comparing of our patterns to ones calculated from the structural files: CIF#9008749 for TiO, CIF#1532065 for $R\bar{3}c$ Ti_2O_3, CIF#9009086 for anatase TiO_2, and CIF# 9009083 for rutile TiO_2 (COD database). CIF file for *Immm* Ti_2O_3 was created following the data of Li et al. [11].

The lowest oxygen content leads to the formation of α-TiO, sample (a). All observed XRD peaks correspond to the cubic NaCl structure with a lattice constant of a = 4.16 Å, which is similar to the value previously reported for the bulk, 4.165 Å [27]. Since the first order Raman scattering is not possible in such structure, we see no well-defined peaks in Figure 5a. The Raman spectrum of this phase is characterized by a very broad feature centered around 220 cm^{-1} and an additional low-intensity broad line around 510 cm^{-1}. The average crystallographic domain size is 33 nm.

Increasing the oxygen amount leads to the deposition of an α-TiO / *Immm* Ti_2O_3 mixture. The new phase is detected by the appearance of small XRD peaks around 2θ = 40.7°, 45.2°, 58.6°, 65.5°, and others. The further increase of oxygen content adds $R\bar{3}c$ Ti_2O_3 into the film and we can see the mixture of three phases as shown in Figure 4b. Using Raman spectroscopy it is difficult to distinguish between magnetron-sputtered TiO and *Immm* Ti_2O_3 films since the polycrystallinity only leads to broad features (compare Figure 5a and Figure 7a). *Immm* Ti_2O_3 is characterized by a more prominent intensity drop in the range of 340-380 cm^{-1}, that we can

clearly see in Figure 5b, thus suggesting the presence of this phase. Two main features of $R\bar{3}c$ Ti_2O_3 can be found around 214 and 250 cm^{-1}.

Increasing the oxygen partial pressure during growth, first eliminates α-TiO (leaving a mixture of two Ti_2O_3 phases), followed by the formation of pure $R\bar{3}c$ Ti_2O_3 described in above.

More oxygen gradually decreases the amount of $R\bar{3}c$ Ti_2O_3 and the intensity of corresponding Raman lines (Figure 5c, d). The new Raman features are very broad and have low-intensities indicating the amorphous nature of such films. A small peak around 140 cm^{-1} could correspond to the formation of low-quality anatase TiO_2. It is confirmed by an XRD peak located around $2\theta = 25.5°$ ((101) anatase plane, Figure 4d). A nearby peak at $2\theta = 28.2°$ corresponds to the signal of rutile TiO_2. The both peaks are very broad confirming the poor crystallinity of the films, both anatase and rutile phases have a coherent domain size on the order of 10 nm. The further decrease of oxygen diminishes all signals from the anatase phase.

3.3. Titanium oxide films produced by sputtering of Ti_2O_3 target.

Due to the limitations of our sputtering system, the minimum oxygen flow during the deposition was 0.4 sccm (the corresponding oxygen partial pressure was 0.18 μbar). Using that flow resulted in the formation of titanium dioxide, even at the highest powers applied to the target. Thus, all experiments with Ti_2O_3 target were conducted under a pure argon atmosphere.

The samples were produced at different argon flows (chamber pressures from 3.3 to 5.3 μbar), substrate temperatures (from 550 to 820 °C), deposition times (from 5 to 60 minutes), and applied power types (DC or RF). In all cases we detected only the formation of *Immm* Ti_2O_3 phase and the typical XRD pattern for such film is given in Figure 6.

All peaks observed for our samples could be attributed to *Immm* structure with the lattice constants of $a = 8.39 \pm 0.01$ Å, $b = 4.43 \pm 0.01$ Å and $c = 2.85 \pm 0.01$ Å. The growth conditions had no effect on the structure of the produced material. Compared to the epitaxial films on sapphire [11], there is a significant discrepancy in the value of *a*-parameter (8.39 Å instead of 9.39 Å). Average crystallographic domain size, as calculated using the Scherrer equation is

approximately 70 nm. This value is higher than that observed in the previously discussed reactively grown films.

The further confirmation of the significant structural difference between epitaxial and magnetron sputtered films is obtained by Raman spectroscopy. Epitaxial films demonstrate four main features located around 240, 330, 440, and 605 cm^{-1}, Figure 7c. Arc sputtered films have the similar response, Figure 7b. All Raman spectra in Figure 7 have the similar background with a sharp decrease of intensity around 350 cm^{-1}. There is a small feature around 320–330 cm^{-1} for magnetron sputtered films, but there are no peaks around 240, 440 or 605 cm^{-1}. Instead, there is a broad feature around 210 cm^{-1}.

The electrical characterization of magnetron sputtered *Immm* Ti_2O_3 films revealed no specific features for our material, see Figure 8b. The conductivity steadily increases with the temperature increase and no transition from semiconducting to metallic state was observed. It is different from the epitaxial films on sapphire where such transition was found around 370 K [11]. Moreover, the absolute value of resistivity for our material is 5–15 times higher that could be due to the different structure of the films. Interestingly, if we compare magnetron sputtered *Immm* and $R\bar{3}c$ Ti_2O_3 films, we see no difference in temperature dependence and values of resistivity above 150 K (Figure 8a, b).

Additional experiments with Ti_2O_3 target were performed at very low substrate temperatures. Surprisingly, below 200°C we detected the formation of titanium monoxide. Compared to reactively sputtered TiO, the lattice constant of such films was slightly increased: a = 4.22 – 4.23 Å, see Figure 9.

This result indicates the non-stoichiometric transfer of the material from the Ti_2O_3 target to the substrate. The oxygen is lost during the sputtering; however, higher temperatures promote the oxidation of the growing titanium oxide film by the residual gas in the vacuum chamber. At higher temperatures the oxidation rate is fast enough to convert monoxide to *Immm* Ti_2O_3.

None of the Ti_2O_3 films deposited by reactive magnetron sputtering from a metallic Ti

target or pure Ar sputtering from a Ti_2O_3 target exhibited the metallic to semiconducting transition characteristic of the material. Corundum-type Ti_2O_3 appears to be frozen in the metallic state regardless of temperature. The semiconductor to metal transition in Ti_2O_3 is driven by the increase of the Ti-bond length with temperature. As our films show distinct texture changes relative to the bulk (reduced *a*, increased *c*), we hypothesize that our Ti-Ti is always above this critical point and that results in the exhibition of metallic properties even at low temperatures.

4. Conclusions

Using the magnetron sputtering system, we produced thin films of different titanium oxide phases, including TiO_2, Ti_2O_3 and TiO. The structure of all samples was determined by X-ray diffraction and Raman spectroscopy. We showed that corundum type Ti_2O_3 films significantly differ from the bulk. Particularly, that results in the absence of semiconductor to metal transition due to the locking in of the film into the metallic regime for all temperatures. Electrical properties of our material demonstrated no specific features and its conductivity corresponded to the conductivity of the bulk crystals in the metallic state. This may be due to both the differences in the crystallography and texturing which may lead to the Ti-Ti bond length being above the threshold distance for all temperatures investigated. We also demonstrated the formation of another Ti_2O_3 phase crystallized at *Immm* space group. The structure of such films again differ from the structure of the same material reported earlier. In summary, our work presents the important data about growth and characterization of titanium suboxides thin films.

Acknowledgements

This publication was made possible with the funds from 5 top 100 Russian Academic Excellence Project at the Immanuel Kant Baltic Federal University and Erasmus+ mobility project. This work was also supported by Science Foundation Ireland (SFI) under Grant Number SFI/12/RC/2278 and 12/IA/1264.

References

[1] G. Lunde, Über Titansesquioxyd, Z. Anorg. Allg. Chem. 164 (1927), 341–344. doi:10.1002/zaac.19271640131

[2] C.E. Rice, W.R. Robinson, Structural changes associated with the semiconductor-to-metal transition in Ti_2O_3, Mater. Res. Bull. 11 (1976) 1355–1359. doi:10.1016/0025-5408(76)90045-3.

[3] S.H. Shin, R.L. Aggarwal, B. Lax, Raman scattering in Ti_2O_3-V_2O_3 alloys, Phys. Rev. B 9 (1974) 583–590. doi:10.1103/PhysRevB.9.583

[4] J.M. Honig, T.B. Reed, Electrical properties of Ti_2O_3 single crystals, Phys. Rev. 174 (1968) 1020–1026. doi:10.1103/PhysRev.174.1020.

[5] H.L. Barros, G. V. Chandrashekhar, T.C. Chi, J.M. Honig, R.J. Sladek, Specific heat of single-crystal undoped and V-doped Ti_2O_3, Phys. Rev. B. 7 (1973) 5147–5192. doi:10.1103/PhysRevB.7.5147.

[6] T.C. Chi, R.J. Sladek, Elastic constants and the electrical transition in Ti_2O_3, Phys. Rev. B 7 (1973) 5080–5085. doi:10.1103/PhysRevB.7.5080

[7] A.D. Pearson, Studies on the lower oxides of titanium, J. Phys. Chem. Solids. 5 (1958) 316–327. doi:10.1016/0022-3697(58)90035-0.

[8] J. Wang, Y. Li, L. Deng, N. Wei, Y. Weng, S. Dong, D. Qi, J. Qiu, X. Chen, T. Wu, High-performance photothermal conversion of narrow-bandgap Ti_2O_3 nanoparticles, Adv. Mater. 29 (2017) 1603730. doi:10.1002/adma.201603730.

[9] D. Nishio-Hamane, M. Katagiri, K. Niwa, A. Sano-Furukawa, T. Okada, T. Yagi, A new high-pressure polymorph of Ti_2O_3: implication for high-pressure phase transition in sesquioxides, High Pressure Res. 29 (2009) 379–388. doi: 10.1080/08957950802665747

[10] S.V. Ovsyannikov, X. Wu, V.V. Shchennikov, A.E. Karkin, N. Dubrovinskaia, G. Garbarino, L. Dubrovinsky, Structural stability of a golden semiconducting orthorhombic polymorph of Ti_2O_3 under high pressures and high temperatures, J. Phys. Condens. Matter. 22

(2010) 375402. doi:10.1088/0953-8984/22/37/375402.

[11] Y. Li, Y. Weng, X. Yin, X. Yu, S.R.S. Kumar, N. Wehbe, H. Wu, H.N. Alshareef, S.J. Pennycook, M.B.H. Breese, J. Chen, S. Dong, T. Wu, Orthorhombic Ti_2O_3: A polymorph-dependent narrow-bandgap ferromagnetic oxide, Adv. Funct. Mater. 28 (2018) 1705657. doi:10.1002/adfm.201705657.

[12] P. Shvets, K. Maksimova, M. Demin, O. Dikaya, A. Goikhman, Cathodic arc sputtering of functional titanium oxide thin films, demonstrating resistive switching, Phys. B Condens. Matter. 513 (2017) 15–20. doi:10.1016/j.physb.2017.02.035.

[13] M. Toyoda, T. Yano, B. Tryba, S. Mozia, T. Tsumura, M. Inagaki, Preparation of carbon-coated Magneli phases Ti_nO_{2n-1} and their photocatalytic activity under visible light, Appl. Catal. B Environ. 88 (2009) 160–164. doi:10.1016/j.apcatb.2008.09.009.

[14] S. Andersson, B. Collén, U. Kuylenstierna, A. Magnéli, H. Pestmalis, S. Åsbrink, Phase analysis studies on the titanium-oxygen system., Acta Chem. Scand. 11 (1957) 1641–1652. doi:10.3891/acta.chem.scand.11-1641.

[15] M. Radecka, A. Trenczek-Zajac, K. Zakrzewska, M. Rekas, Effect of oxygen nonstoichiometry on photo-electrochemical properties of TiO_{2-x}, J. Power Sources 173 (2007) 816–821. doi:10.1016/j.jpowsour.2007.05.065.

[16] M. Wajid Shah, Y. Zhu, X. Fan, J. Zhao, Y. Li, S. Asim, C. Wang, Facile synthesis of defective TiO_{2-x} nanocrystals with high surface area and tailoring bandgap for visible-light photocatalysis, Sci. Rep. 5 (2015) 15804. doi:10.1038/srep15804.

[17] L.R. Grabstanowicz, S. Gao, T. Li, R.M. Rickard, T. Rajh, D.J. Liu, T. Xu, Facile oxidative conversion of TiH_2 to high-concentration Ti^{3+}-self-doped rutile TiO_2 with visible-light photoactivity, Inorg. Chem. 52 (2013) 3884–3890. doi:10.1021/ic3026182.

[18] A. Teleki, S.E. Pratsinis, Blue nano titania made in diffusion flames, Phys. Chem. Chem. Phys. 11 (2009) 3742–3747. doi:10.1039/b821590a.

[19] G.S. Chen, C.C. Lee, H. Niu, W. Huang, R. Jann, T. Schütte, Sputter deposition of titanium

monoxide and dioxide thin films with controlled properties using optical emission spectroscopy, Thin Solid Films 516 (2008) 8473–8478. doi:10.1016/j.tsf.2008.04.093.

[20] E.C. Fredriksson, J.-O. Carlsson, Chemical vapour deposition of TiO and Ti_2O_3 from $TiCl_4/H_2/CO_2$ gas mixtures, Surf. Coatings Technol. 73 (1995) 160–169. doi:http://dx.doi.org/10.1016/0257-8972(94)02378-6.

[21] M.N. Simcock, Thin film growth of TiO_2 and Ti_2O_3 by the new method of liquid injection CVD investigated using optical interferometry, XRD and AFM, Surf. Interface Anal. 38 (2006) 1122–1129. doi:10.1002/sia.2359.

[22] S. Graulis, D. Chateigner, R.T. Downs, A.F.T. Yokochi, M. Quirós, L. Lutterotti, E. Manakova, J. Butkus, P. Moeck, A. Le Bail, Crystallography Open Database – An open-access collection of crystal structures, J. Appl. Crystallogr. 42 (2009) 726–729. doi:10.1107/S0021889809016690.

[23] Y. Tsujimoto, Y. Matsushita, S. Yu, K. Yamaura, T. Uchikoshi, Size dependence of structural, magnetic, and electrical properties in corundum-type Ti_2O_3 nanoparticles showing insulator-metal transition, J. Asian Ceram. Soc. 3 (2015) 325–333. doi:10.1016/j.jascer.2015.06.007.

[24] S.H. Shin, F.H. Pollak, T. Halpern, P.M. Raccah, Resonance Raman scattering in Ti_2O_3 in the range 1.8–2.7 eV, Solid State Commun. 16 (1975) 687–690. doi:10.1016/0038-1098(75)90453-6.

[25] V. Singh, J.J. Pulikkotil, Electronic phase transition and transport properties of Ti_2O_3, J. Alloys Compd. 658 (2016) 430–434. doi:10.1016/j.jallcom.2015.10.203.

[26] S.H. Shin, G. V. Chandrashekhar, R.E. Loehman, J.M. Honig, Thermoelectric effects in pure and V-doped Ti_2O_3 single crystals, Phys. Rev. B 8 (1973) 1364–1373. doi:10.1103/PhysRevB.8.1364.

[27] P. Ehrlich, Phasenverhältnisse und Magnetisches Verhalten im System Titan/Sauerstoff, Z. Elektrochem. Angew. P. 45 (1939) 362–370. doi:10.1002/bbpc.19390450506.

List of figure and table captions

Figure 1. XRD pattern of stoichiometric Ti_2O_3 film produced by reactive magnetron sputtering on glass substrate.

Figure 2. Raman spectrum of stoichiometric Ti_2O_3 film produced by reactive magnetron sputtering.

Figure 3. The dependence of resistivity on the temperature: (a) magnetron-sputtered Ti_2O_3 film, (b) Ti_2O_3 bulk [26].

Figure 4. XRD patterns of the selected TiO_x films (logarithmic scale). Asterisks mark the positions of the substrate holder peaks. □ – α-TiO, ◊ – *Immm* Ti_2O_3, ○ – $R\bar{3}c$ Ti_2O_3, r – rutile TiO_2, a – anatase TiO_2. An intense peak at $2\theta = 69.16°$ for sample (b) is due to the Si (100) substrate; other samples are deposited on glass. The oxidation rate is increased from sample (a) to sample (d), the synthesis conditions are listed in Table 1.

Figure 5. Raman spectra of the selected TiO_x films: (a) α-TiO, (b) α-TiO + *Immm* Ti_2O_3 + $R\bar{3}c$ Ti_2O_3, (c) $R\bar{3}c$ Ti_2O_3, (d) $R\bar{3}c$ Ti_2O_3 + rutile TiO_2 + anatase TiO_2.

Figure 6. XRD pattern of the sample produced from Ti_2O_3 target on glass substrate. Asterisks mark the positions of the substrate holder peaks.

Figure 7. Raman spectra of *Immm* Ti_2O_3 films: (a) magnetron sputtered film on glass substrate [this work]; (b) thin arc sputtered film on the silicon substrate [12] (asterisks mark the positions of the silicon substrate peaks); (c) epitaxial film on sapphire [11].

Figure 8. The dependence of resistivity on the temperature (logarithmic scale): (a) magnetron-sputtered *Immm* Ti_2O_3 film, (b) magnetron-sputtered $R\bar{3}c$ Ti_2O_3 film (c) epitaxial *Immm* Ti_2O_3 film [11].

Figure 9. XRD patterns for TiO films produced from Ti_2O_3 target at different substrate temperatures: (a) 40 °C, (b) 200 °C, and by reactive sputtering of Ti target at 550 °C (c). Asterisks mark the positions of the substrate holder peaks.

Table 1. Growth parameters of the selected TiO_x films.

Tables (if any)

sample	substrate temperature, °C	oxygen pressure, µbar	growth rate, nm/min
(a)	550	0.18	12.7
(b)	780	0.18	11.2
(c)	550	0.28	14.7
(d)	550	0.30	14.3

Figures (if any)

Click here to download high resolution image

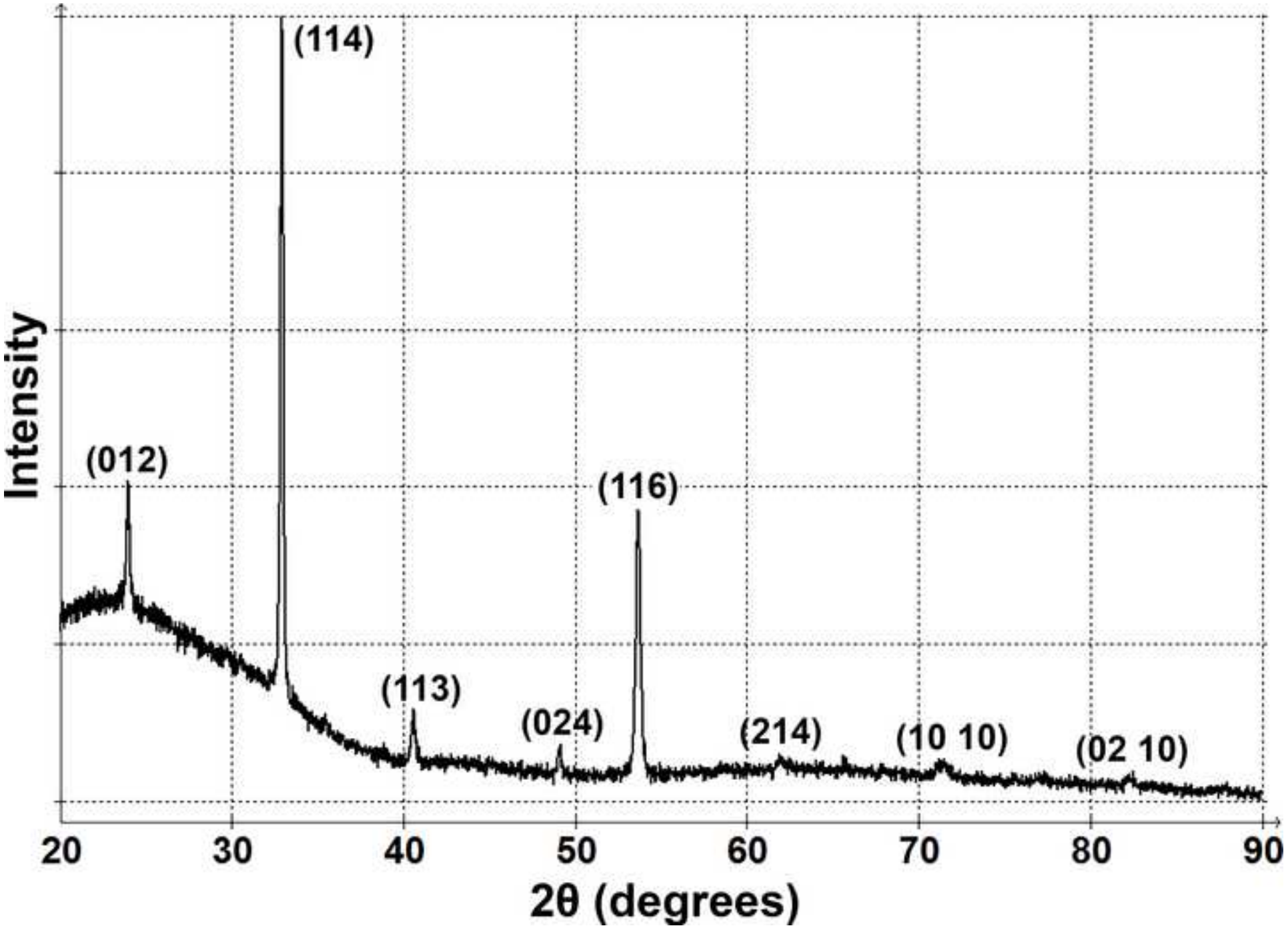

Figures (if any)

Click here to download high resolution image

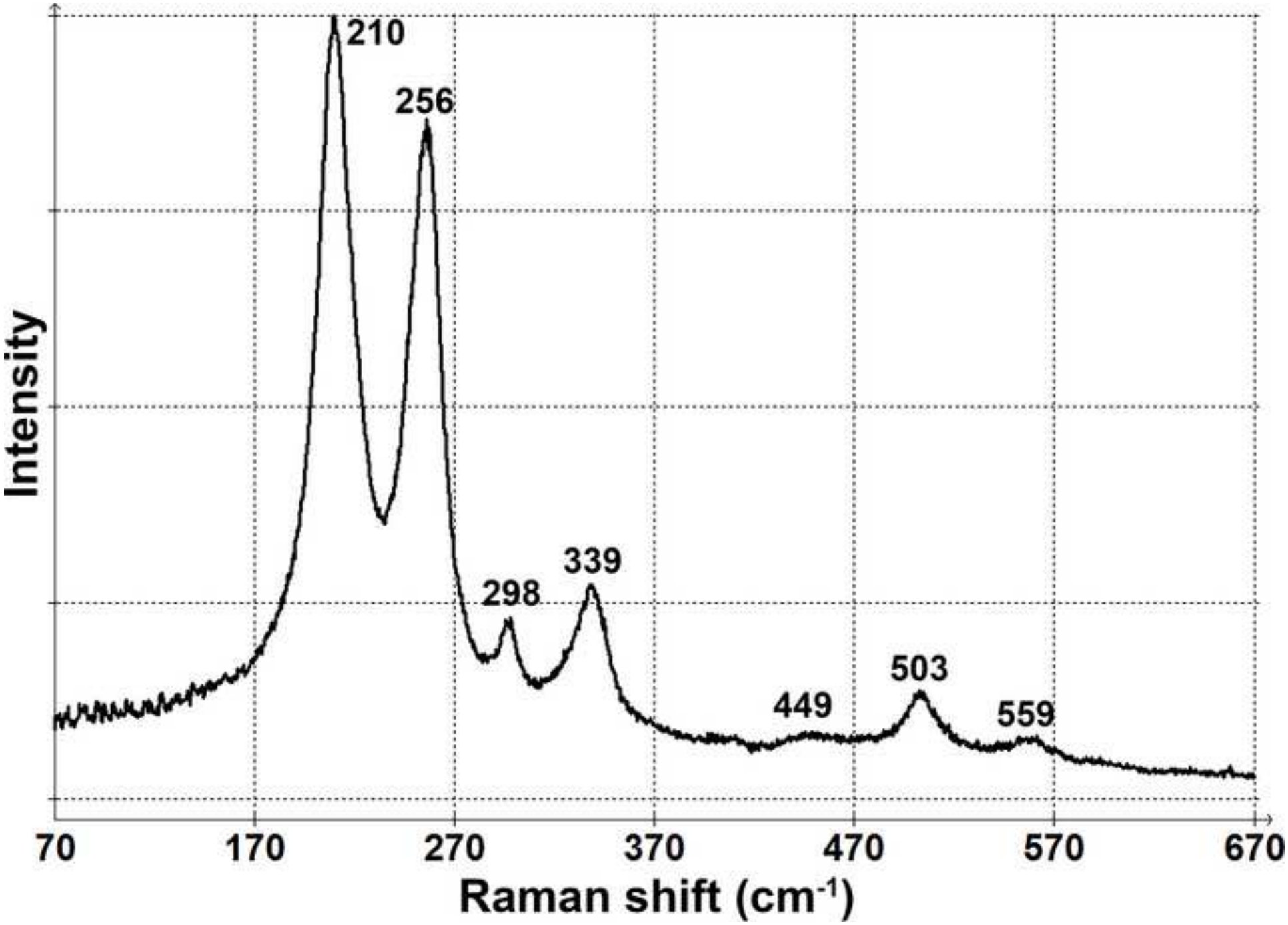

Figures (if any)

Click here to download high resolution image

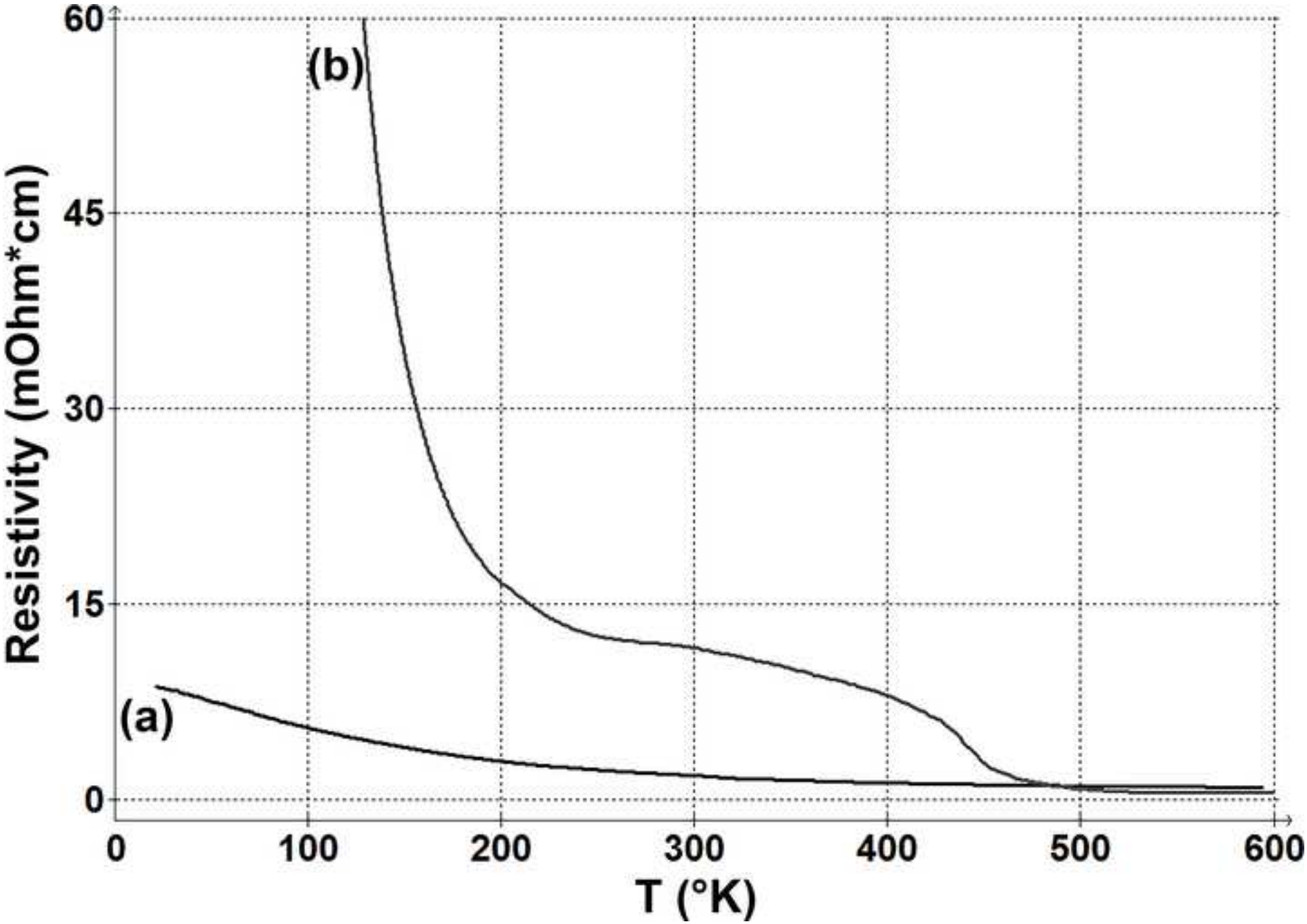

Figures (if any)

Click here to download high resolution image

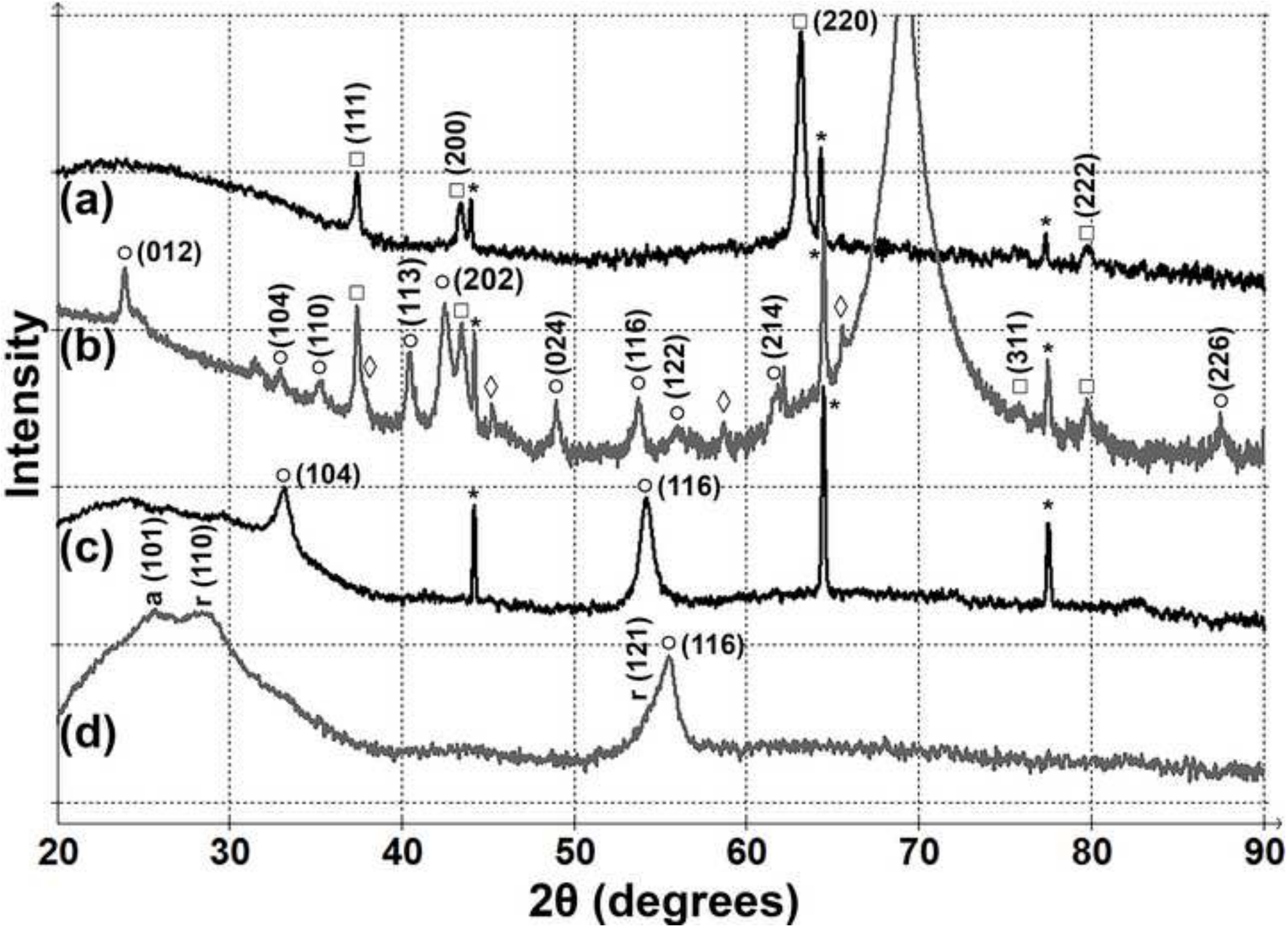

Figures (if any)

Click here to download high resolution image

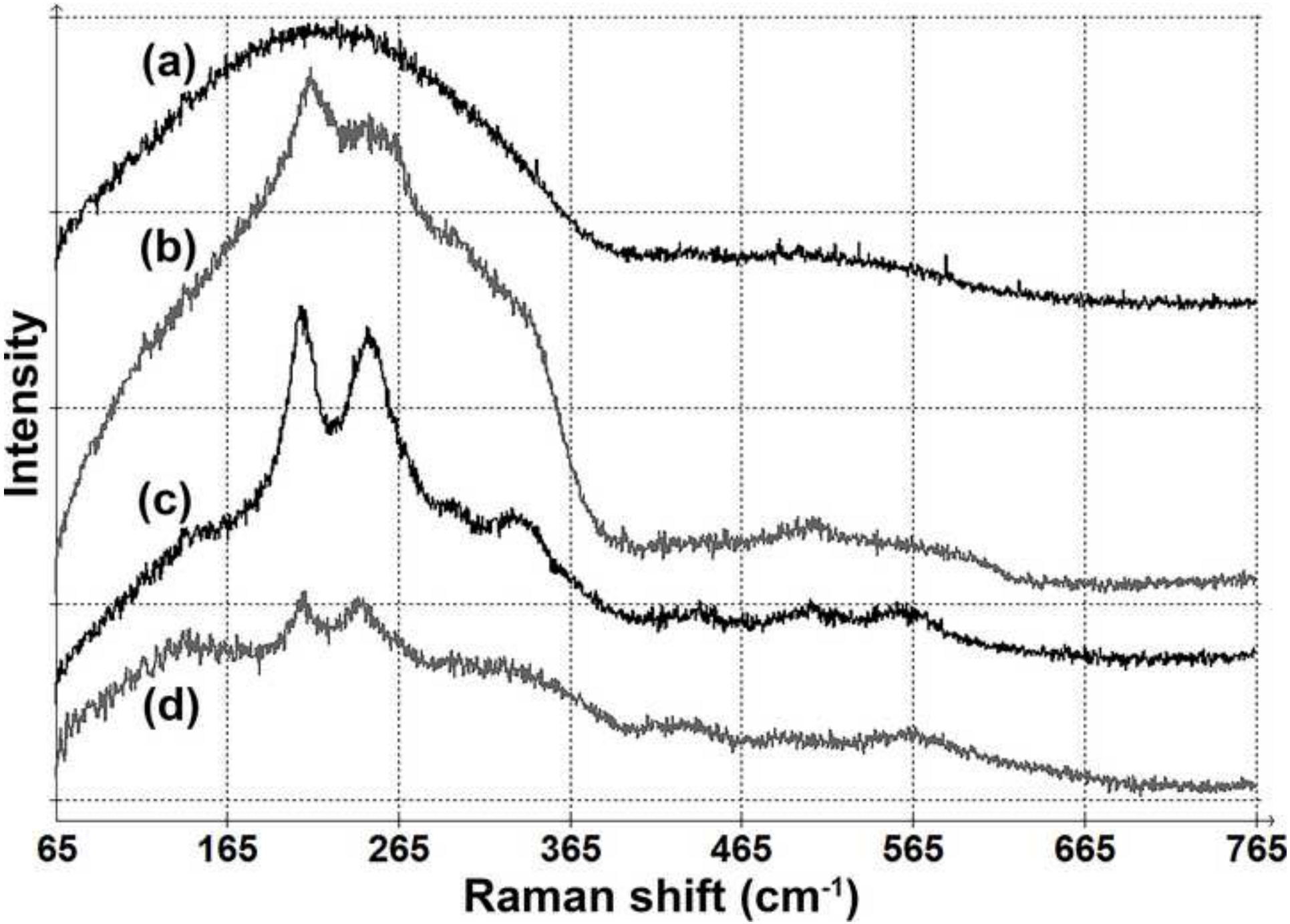

Figures (if any)

Click here to download high resolution image

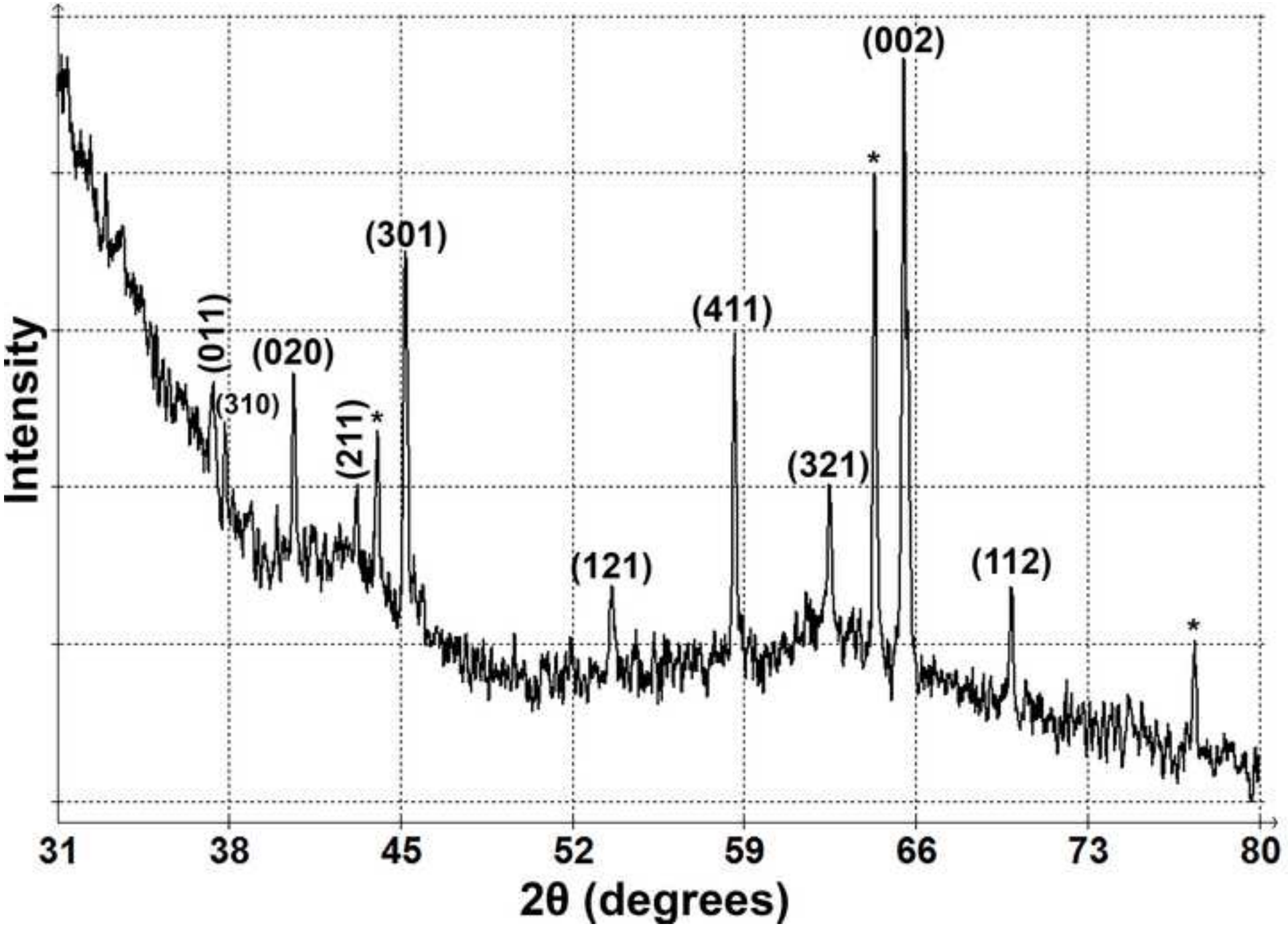

Figures (if any)

Click here to download high resolution image

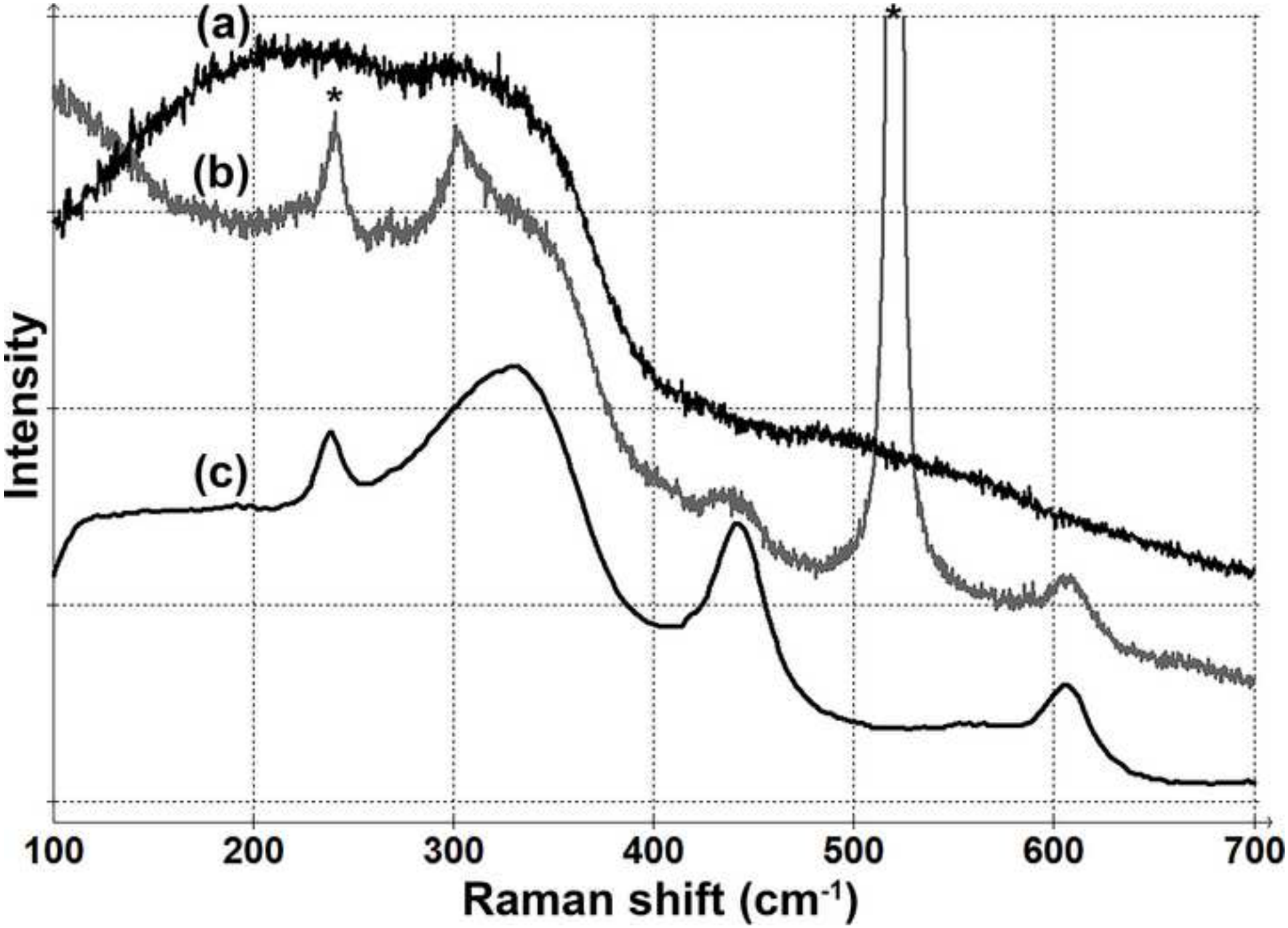

Figures (if any)

Click here to download high resolution image

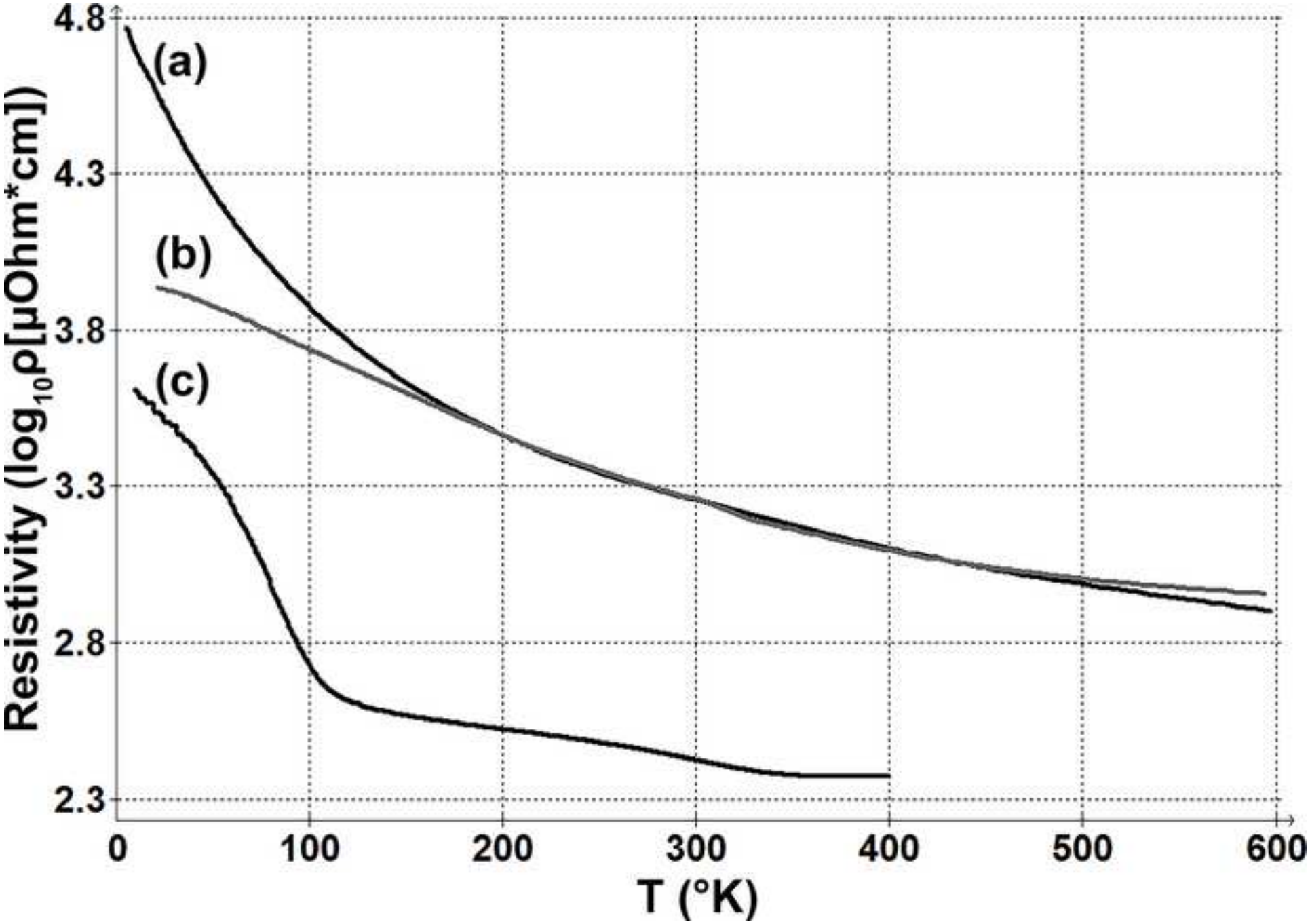

Figures (if any)

Click here to download high resolution image